Wavefront Measurements of a Supersonic Boundary Layer Using a Laser-Induced Breakdown Spark

R. Mark Rennie[1], Minh Nguyen[2], Stanislav Gordeyev[3], Eric J. Jumper[4]
University of Notre Dame, Notre Dame, Indiana, 46545

Alan B. Cain[5]
Innovative Technology Applications Co., Chesterfield, MO, 63006

Timothy E. Hayden[6]
U.S. Air Force Academy, Colorado Springs, Colorado 80840

The aero-optical effect of a flat-plate adiabatic boundary layer has been measured using the light generated by a laser-induced breakdown (LIB) spark. The measurements were performed in a blowdown wind tunnel at freestream Mach numbers of 3 and 4.38. The tests showed that the aero-optical effect of boundary layers with OPD_{rms} as low as 0.05 μm could be accurately measured using the LIB spark, including their deflection-angle spatial spectra. The results demonstrate that using the LIB spark as a source of illumination, it is possible to make accurate measurements of low-amplitude aero-optical effects in a manner that is self-contained, non-intrusive, and suitable for a flight-test environment.

Nomenclature

C_f	=	skin friction coefficient	P_t	=	total pressure
δ	=	boundary layer thickness	θ	=	small-aperture deflection angle
d_{AP}	=	measurement aperture diameter	$\hat{\theta}$	=	deflection angle spectrum
d_L	=	lenslet size	ρ	=	density
D_L	=	laser lens aperture	r	=	radial coordinate
E	=	pulse energy	rms	=	root-mean-square
f_c	=	collimating lens focal length	St_δ	=	Strouhal number based on δ
f_L	=	laser lens focal length	t	=	time
k	=	streamwise wavenumber	U_c	=	disturbance convection velocity
K_{GD}	=	Gladestone-Dale constant	U_∞	=	freestream speed
λ	=	disturbance wavelength	W	=	wavefront
λ_L	=	laser wavelength	x	=	streamwise coordinate
M_∞	=	Mach number	y	=	cross-stream coordinate
n	=	index of refraction	Z_C	=	Zernike coefficient
OPD	=	optical path difference			

[1] Research Associate Professor, Department of Mechanical and Aerospace Engineering, Hessert Laboratory for Aerospace Research, Notre Dame, IN 46556, Senior Member AIAA.
[2] Graduate Research Assistant, Department of Mechanical and Aerospace Engineering, Hessert Laboratory for Aerospace Research, Notre Dame, IN 46556, Student Member AIAA.
[3] Associate Professor, Department of Mechanical and Aerospace Engineering, Hessert Laboratory for Aerospace Research, Notre Dame, IN 46556, Associate Fellow AIAA.
[4] Professor, Department of Mechanical and Aerospace Engineering, Hessert Laboratory for Aerospace Research, Notre Dame, IN 46556, Fellow AIAA.
[5] President, Innovative Technology Applications Company, Chesterfield, MO 63006, Associate Fellow AIAA.
[6]Aerospace Engineer, Department of Aeronautics, Senior Member AIAA.

I. Introduction

THE wavefront of a beam of light passing through a compressible flow is distorted by spatial and temporal variations of the refractive index within the flow. The refractive-index variations are related to density variations by the Gladstone-Dale relationship:

$$n(\vec{x},t) = 1 + K_{GD}\rho(\vec{x},t) \tag{1}$$

where the Gladstone-Dale constant K_{GD} has a value of approximately $2.27\text{x}10^{-4}$ m^3/kg for light at visible and near-IR wavelengths. The optical distortion on a beam of light transiting the flow is then the average-removed integral of n along the distance traversed by the light beam:

$$OPD(x,y,t) = \int n'(x,y,z,t)dz \tag{2}$$

where *OPD* is the optical path difference, prime denotes mean-removed fluctuations, and propagation in the *z* direction is assumed. The study of the optical effect of compressible flows is called "aero optics." Examples of recent investigations into the aero-optical effects of boundary layers, shear layers and shock waves are described in [1-6].

Aero-optical effects are most commonly studied to evaluate their effect on airborne optical systems including directed-energy, imaging, or free-space communications systems. However, since the aberrations are the integrated effect of the flow density field, aero-optical measurements can also be used to extract information on the underlying flow itself. As shown in [1-3], a flight-test measurement of the optical aberration imposed by the (turbulent) vehicle boundary layer can be used to estimate boundary-layer thickness δ, local convection velocity, density, and other boundary-layer parameters; this kind of fluid-mechanic understanding cannot always be obtained from ground-test and computational fluid dynamics (CFD) efforts alone.

Flight-test measurements of the aero-optical effect of a vehicle boundary layer (or other turbulent flow) are complicated by the need for a source of light to provide the interrogating wavefront, that can be reliably generated at different locations in the flow. One approach to solving this problem is to use an artificial light source for aero-optical measurements that is generated by focusing the output of a laser to create a laser-induced breakdown (LIB) spark. In this case, the broadband emission from the LIB is passed through the aero-optical flow of interest and into a wavefront sensor to detect the optical effect of the flow. The advantages of this approach are that the LIB can be formed at any location around the aircraft without the need for mounts or appendages that might perturb the aero-optical flow of

interest. A layout of a conceptual instrument to measure the aero-optical effect of the boundary layer on a flight-test vehicle is shown in Fig. 1; such an instrument is both fully self-contained and nonintrusive.

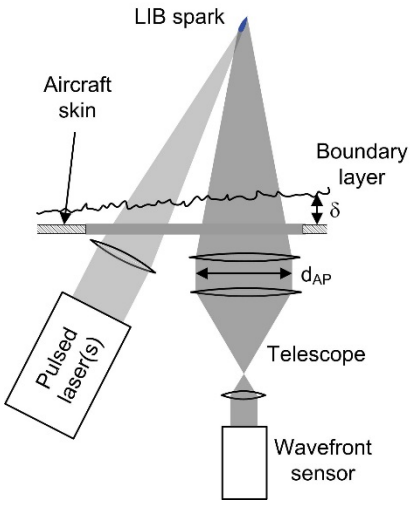

Fig. 1. Basic concept for instrument to measure aero-optical effect of aircraft boundary layer in flight.

It should be emphasized that the purpose of the LIB in Fig.1 is to generate a near-point source of light for measurement of the aero-optical flow of interest and not, for example, to investigate the behavior or composition of the LIB itself. In this regard, previous literature on this kind of "aero-optical guide star" is sparse [7-10]. Although "laser guide stars" are commonly used to evaluate atmospheric optical effects on ground-based telescopes [11], these techniques are based on Raleigh scattering or sodium fluorescence and do not involve LIB. In [7], the requirements for LIB measurements of aero-optical flows at hypersonic flow speeds is reviewed but detailed wavefront data are not shown. In our previous work described in [8-10], the output of a pulsed Nd:YAG laser with wavelength of 355 nm was focused to create a LIB spark which was successfully used to measure the aero-optical aberrations produced by a compressible shear-layer flow. However, due to the small scale of the wind tunnel used in these investigations, the LIB spark was formed in the quiescent laboratory air outside of the wind tunnel with the generated light directed through the wind-tunnel test section and shear-layer flow; as such, the test did not fully simulate the conditions of an actual flight-test deployment. Furthermore, although the tests showed that the optical aberration of the shear layer could be accurately measured using the technique, the optical effect of the shear layer was quite large so that the tests did not demonstrate the kind of measurement accuracy that can be achieved.

In this article the results of an effort to measure the aero-optical effect of a compressible boundary layer using the light from a LIB spark are presented. The measurements were performed at high supersonic Mach numbers and are

novel in the sense that the LIB spark was generated in the flow and therefore more faithfully simulates an actual flight-test deployment of the measurement approach. Furthermore, the magnitude of the aero-optical distortion created by the boundary-layer flows under investigation were 1 to 2 orders of magnitude less than the shear-layer flows investigated in [8-10], so that the results of these tests represent a more rigorous demonstration of the level of measurement sensitivity that can be achieved using the technique. New methods to remove measurement noise and improve the sensitivity of the technique are also presented.

II. Experiment

The measurements were performed in the Trisonic Wind Tunnel (TWT) at the US Air Force Academy. This tunnel has a blowdown configuration with test-section dimensions of 1 ft x 1 ft, maximum Mach number of 4.38, and maximum test-section total pressure of 1.7 MPa. Air storage consists of six 25.5 m^3 tanks that can be pumped to a pressure of 4 MPa, giving up to 7 min of total run time depending on test conditions. The stored air is first dried to - 45^{o}C dewpoint, filtered, and then heated to around 38^{o}C in order to prevent water condensation, ice formation and/or liquefaction in the test section.

The measurements were performed at test-section Mach numbers of M_∞ = 3.0 and 4.38. Tunnel conditions for the experiments performed are summarized in Table 1. The flow speeds shown in the table were computed using the storage tank stagnation temperature of 311 K and assuming isentropic flow. The boundary-layer thickness δ and skin friction C_f at the measurement location were estimated from the geometry of the wind-tunnel nozzles using a semi-empirical method described in [12], and δ was also verified by Schlieren measurements. The equivalent standard-atmosphere altitude shown in Table 1 is based on the test-section density, which has the most effect on the magnitude of the aero-optical aberration produced by the boundary layer and hence signal strength of the measurements.

Table 1. Summary of test conditions for LIB spark measurements.

Parameter	Test 1	Test 2	Test 3	Test 4	Test 5
Mach number	4.38	3.0	3.0	3.0	3.0
Total pressure (MPa)	1.5	1.4	1.0	0.7	0.5
Density (kg/m^3)	0.36	1.13	0.86	0.57	0.42
Flow speed (m/s)	704 ± 2	633 ± 2	633 ± 2	633 ± 2	633 ± 2
δ (mm)	26 ± 2.5	16 ± 1.5	16 ± 1.5	16 ± 1.5	16 ± 1.5
Equivalent altitude (km)	11.1	0.8	3.5	7.3	9.7
Laser pulse energy (mJ)	18 – 25 ±2.6	10.6 ±2.6	11.8 ±2.6	12.6 ±2.6	15.8 ±2.6

A. LIB Measurements

A schematic and photograph showing the optical setup for the LIB spark measurements in the TWT test section are shown in Fig. 2. The experiments were performed with an empty test section. A LIB spark was formed near the far wall of the test section by focusing the output of a Nd:YAG pulsed laser with wavelength λ_L = 355 nm and pulse duration Δt = 5 ns through a fused-silica window with good UV transmission properties. The advantage of the 355 nm wavelength is that, since the focal region of the focused laser beam becomes smaller as the wavelength is reduced, breakdown can be achieved with less pulse energy so that smaller LIB sparks can be formed thereby improving the performance of the wavefront measurements [8-10].

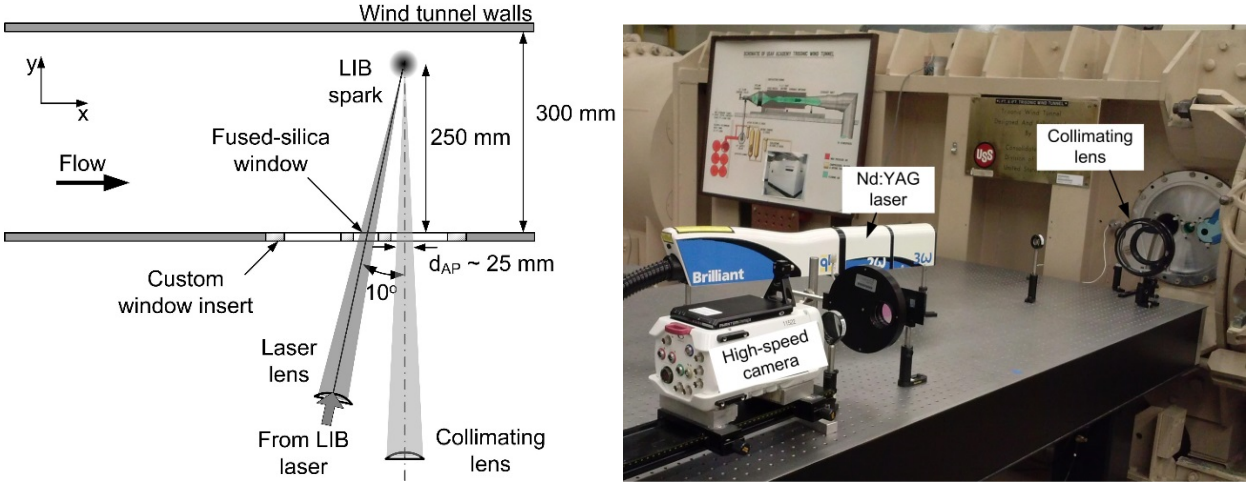

Fig. 2. Schematic (left), and photograph (right), of experiment to measure aero-optical effect of wall boundary layer of the Trisonic Wind Tunnel using return light from an LIB spark.

The laser beam was first expanded to a diameter of 50 mm and focused using a 500 mm focal length lens giving an *f#* for the focused beam of f_L/D_L = 10. Beam pulse energies E just above the breakdown threshold were used to generate the LIB spark, and are shown in Table 1. The mean irradiance at the beam focal point, computed using Eq. (3) [13], was in the range 1.5 to 3 x 10^{13} W/cm^2; these irradiances are comparable to breakdown thresholds reported in, for example, [14]. No flow seeding or other measures were taken to aid the generation of LIB.

$$I = \frac{E}{4\pi\Delta t\left[\frac{\lambda_L f_L}{\pi D_L}\right]^2} \tag{3}$$

After passing through the wall boundary layer of the TWT test section, the light from the LIB spark was collected using a collimating lens (see Fig. 2), passed through a beam reducer, and into a wavefront sensor. The wavefront sensor consisted of a lenslet array with 38.1 mm focal length and 0.3 mm lenslet pitch attached to a high-speed camera. The beam size on the CCD sensor was typically sized to span around 50 lenslets, with pixel resolution of ~15 pixels per lenslet. The sampling frequency of the measurements was 10 Hz, which was dictated by the pulse repetition rate of the Nd:YAG laser. The exposure time of the wavefront-sensor camera was also much longer than the 5 ns pulse duration of the laser, so that the wavefront sensor captured the full emission of the LIB spark. With this setup, the brightness of the LIB spark generated with the pulse energies shown in Table 1 was found to be sufficient for good wavefront measurements.

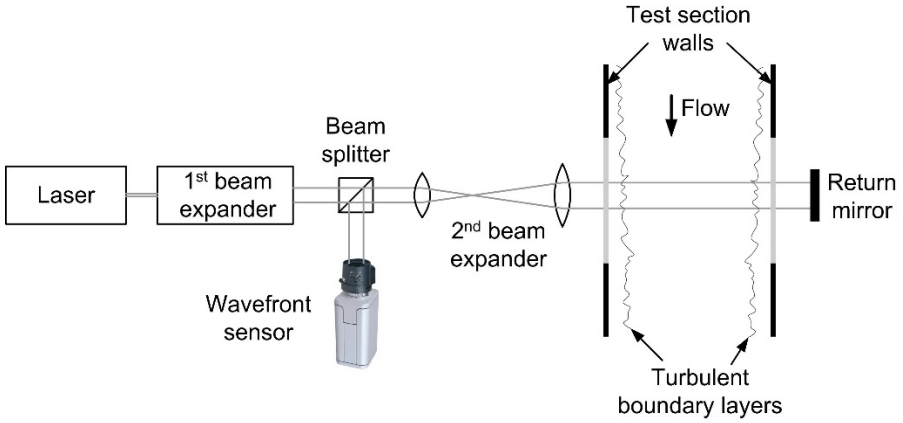

Fig. 3. Schematic of experiment to measure TWT wall boundary-layers aero-optical effect using CW laser.

B. CW Laser Measurements

Wavefront measurements of the TWT boundary layer were also made using a collimated, continuous (CW) laser beam, and used to compare with the data obtained using the LIB spark. A schematic showing the setup for the experiments using the CW laser is shown in Fig. 3. For these tests, a collimated 25 mm diameter, 532 nm wavelength light beam was directed through the empty test section normal to the optical-access windows. A return mirror on the other side of the test section was used to reflect the beam back through the test section and into a wavefront sensor, so that the beam passed through both wall boundary layers twice, amplifying the optical aberration detected by the CW beam by a factor of $2\sqrt{2}$ [1]. The wavefront sensor had the same configuration as the LIB tests, that is, a high-speed camera with a 38.1 mm focal-length lenslet array with 0.3 mm lenslet pitch. CW measurements of the boundary-layer aero-optical effect were performed at test-section conditions corresponding to tests 1 and 3 of Table 1 (M_∞ = 3.0, P_t = 1.0 MPa and M_∞ = 4.38, P_t = 1.5 MPa). Additional information on the CW measurements can be found in [15].

III. Results

Figure 4 shows an example of a single unprocessed image from the wavefront sensor acquired using the LIB spark. Each "dot" in the unprocessed image is formed by a lenslet in the lenslet array and is an image of the LIB spark itself on the wavefront-sensor camera CCD array. Close inspection of Fig. 4 shows that the individual spark images become more elongated towards the edges of the measurement aperture. This elongation is the result of the different aspect of the LIB spark as "viewed" by the individual lenslets in the lenslet array, so that the spark appears elongated in the perspective of the lenslets located on the edge of the aperture. Previous work on how the wavefront measurements are affected by the size and shape of the LIB spark can be found in [10].

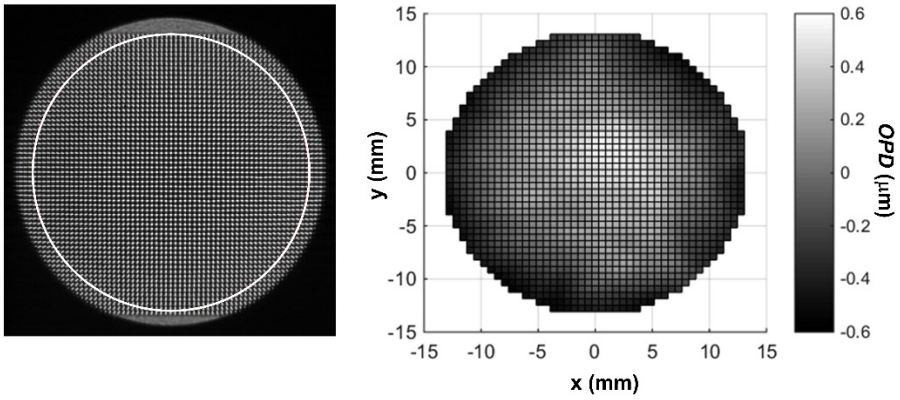

Fig. 4. Typical unprocessed dot pattern (left) from wavefront sensor with circular aperture shown, and sample wavefront (right) computed from apertured dot pattern.

The grey regions at the top and bottom of Fig. 4 are regions of the camera CCD array that were outside of the extent of the lenslet array. These regions were removed by applying a circular aperture with diameter d_{AP} = 25 mm to the dot pattern, see Fig. 4. Wavefronts were then computed from the apertured dot patterns using standard methods. Specifically, "areas of interest" (AOIs) were defined around each dot (i.e. spark image) in the raw camera images after which dot locations were determined using a first-order centroiding algorithm [16]. Reference locations for the dots were then computed as the average over all images for a given test, and wavefront slopes were computed based on the dot deflections from their reference locations. Wavefronts were reconstructed from the wavefront slopes using the Southwell method [17], and optical tip, tilt and piston were removed from the wavefronts using a least-squares plane fitting calculation. Figure 4, right, shows a typical wavefront computed using this methodology.

A. Compensation for Spark Motion Effect

A consequence of using the LIB spark for wavefront measurements is that the resulting wavefronts can be altered by the effect of motions of the LIB spark itself. As shown in [10], these motion-induced variations of the LIB spark wavefront are produced even in still air, where in this case the spark motions are produced by small displacements in the exact location of the LIB spark and/or variations in the shape of the spark between spark ignitions. Since the wavefront for an individual measurement is computed from the displacements of the raw dot locations from the reference dot locations (that were ensemble-averaged over multiple measurements, see Fig. 4 and preceding explanation), small variations in the spark shape or effective location for an individual measurement can alter the dot pattern and resulting wavefront in a manner that is unrelated to the aero-optical effect of the flow under test.

A distinction between the current study and the previous results reported in [10] is that spark motion could also have been produced by convection of the spark with the tunnel flow, which moved at a speed of up to 704 m/s in a direction perpendicular to the line of sight of the wavefront measurements, see Table 1 and Fig. 2. As shown in [18], if laser pulse energies significantly greater than the breakdown threshold are used, the spark can have a lifetime (i.e. the time duration over which the spark emission is detectable by the wavefront-sensor camera) that is significantly longer than the laser pulse duration and on the order of several microseconds. However, for the LIB wavefront measurements described here, the laser pulse energy was reduced to the minimum level that produced raw dot patterns that were just bright enough for accurate measurements; as such, the effective spark lifetime was likely much shorter and on the order of 1 μs or less. More importantly, it is worth repeating that it is the spark-to-spark *variation* of the spark convected motion from the mean that produces the motion-induced LIB aberration, which is much less than the absolute convected motion. Finally, as shown by the optical setup in Fig. 2, the convected motion of the spark was perpendicular to the wavefront-sensor line of sight so that the LIB convected motion would be expected to produce primarily optical tip/tilt, which was not used in the current study and was discarded from the data (see above). In summary, although no attempt was made to evaluate it in detail, it is possible that the convected motion of the LIB spark could also have had an effect on the wavefront results, but this effect was likely much smaller than the variations in spark location that occur even in still air and are reported in [10].

In [10] it was shown that the motion-related wavefront distortions of the spark emitted light are primarily characterized by the Zernike defocus mode [19] with a small amount of comatic aberration also present. Figure 5 [10] illustrates how Zernike defocus arises from small displacements ε of the spark towards or away from the focal point

of the lens used to collimate the spark emitted light; referring to Fig. 4 it is seen that the sample LIB wavefront clearly shows a significant defocus component. Note that aberrations including defocus, coma, etc. could also conceivably have been added to the measured wavefronts by imperfections in the optical setup used to collect and direct the spark light into the wavefront sensor; however, again these aberrations are non-variant from measurement to measurement and are effectively "zeroed out" when the reference dot locations are computed via the averaging of multiple measurements.

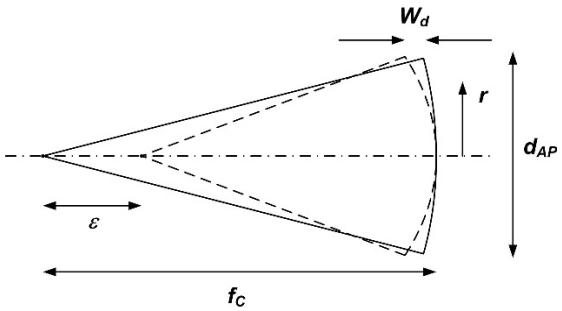

Fig. 5. Schematic showing how small displacements ε of the LIB spark towards or away from the collimating lens produce residual defocus on the measured wavefront [10].

Based on the findings of [10], a Zernike decomposition of the wavefronts measured using the LIB spark was performed. The result for a typical data set is plotted in Fig. 6, which shows the magnitudes of the first 40 Zernike coefficients for wavefronts acquired at $M_\infty = 3$, $P_t = 1.0$ MPa. In Fig. 6, the magnitude of the Zernike coefficient for each mode represents the contribution of that mode to the overall root-mean-square of the spatial wavefront distortion, OPD_{rms}. Included in the figure is an equivalent Zernike decomposition of a set of wavefronts acquired using the CW laser at the same Mach number and using the same size of measurement aperture. Figure 6 clearly shows that the spark wavefronts are affected primarily by defocus (Zernike mode 4) and some coma (mode 7) in agreement with [10]. The results in Fig. 6 also extend upon the findings of [10] by showing that the LIB also produces some astigmatism (mode 6), and by quantifying the magnitude of the LIB effect via comparison with equivalent CW data. Diagrams of the Zernike defocus, astigmatism and coma modes are shown in Fig. 7 for reference.

In [10], it is shown that the OPD_{rms} contributed by the Zernike defocus mode (Z_{C4}) can be related to spark motion ε by:

$$Z_{C4} = \frac{\varepsilon}{27.7\left[\frac{f_C}{D_C}\right]^2} \tag{4}$$

In Eq.(4), f_C/D_C is the *f#* of the collimating lens used to collect the light from the LIB spark, where f_C/D_C=10 for the

LIB wavefront measurements as shown in Fig. 2. Using the result $Z_{C4} \sim 0.1$ μm from Fig. 6 gives $\varepsilon \sim 0.27$ mm. This result corresponds reasonably well with typical variations of spark dimensions reported in [10] and other studies.

In general, wavefront distortions produced by compressible boundary layers and other aero-optical flows are very poorly represented by Zernike modes, as demonstrated by the slow convergence of the Zernike coefficients for the CW wavefronts shown in Fig. 6. This is because the radial and azimuthal symmetries of the Zernike mode shapes fail to capture the dominant streamwise orientation of boundary-layer aero-optical disturbances. As such, a first approach to removing the effect of LIB spark motion is to simply subtract the affected Zernike modes from the measured wavefronts. The top row of Fig. 8 shows a sample of 4 wavefronts acquired using the LIB spark with Zernike modes 4, 6, and 7 removed. The wavefronts in Fig. 8 no longer show the strong defocus mode present in Fig. 4 right, and are much more representative of boundary-layer aero-optical disturbances; specifically, they show dominant optical-structure sizes on the order of the boundary-layer thickness in agreement with boundary-layer aero-optical behavior described in [1-4]. Four wavefronts acquired using CW illumination are also shown in the bottom row of Fig. 8 and show qualitatively similar characteristics and structure sizes to the LIB wavefronts above.

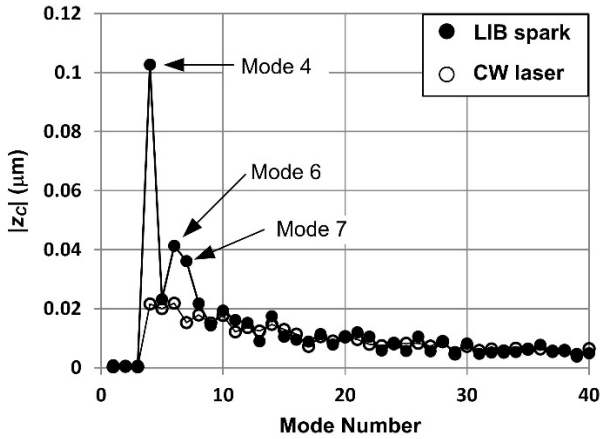

Fig. 6. Zernike coefficient magnitudes for a data set acquired at M_∞ = 3, P_t = 1.0 MPa

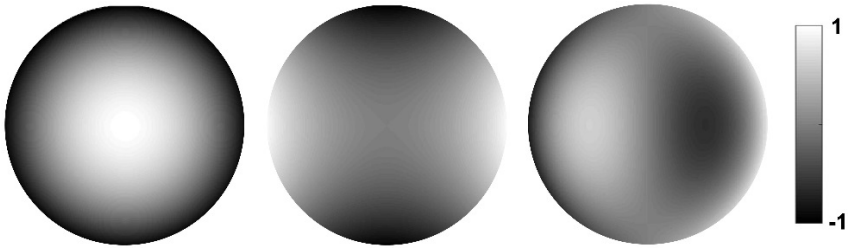

Fig. 7. Nondimensional Zernike modes 4, 6 and 7.

In [1,2] the OPD_{rms} of the aero-optical aberrations produced by a flat-plate adiabatic boundary layer was modeled

using:

$$OPD_{rms} = K_{GD}\rho_\infty M_\infty^2 \delta \sqrt{C_f} F(M_\infty) \tag{5}$$

where $F(M_\infty)$ is an empirical function shown in Fig. 9. In [3], a model for the boundary-layer was developed that had similar functional form to Eq. (5) but with slightly different $F(M_\infty)$ that is also shown in Fig. 9. The OPD_{rms} that was computed for the full-aperture, CW measurements made at M_∞ = 3 and 4.38 were shown to match the models within experimental error, see data points in Fig. 9 [15]. As shown in Table 1, Tests 2 to 5 were performed at M_∞ = 3 but at different total pressures and hence static densities; a plot of the OPD_{rms} for the data acquired using the LIB spark for these tests, and with Zernike modes 4, 6 and 7 removed, is shown in Fig. 10. The figure includes Eq.(5), and shows that the LIB results also match the model within experimental uncertainty. Figures 8 and 10 therefore demonstrate that, after correcting for the Zernike modes imposed by the LIB itself, it is possible to make accurate measurements of boundary-layer optical distortions and OPD_{rms} using the LIB spark at altitudes up to at least the maximum shown in Table 1, where the local air density and hence strength of the optical signal is significantly reduced.

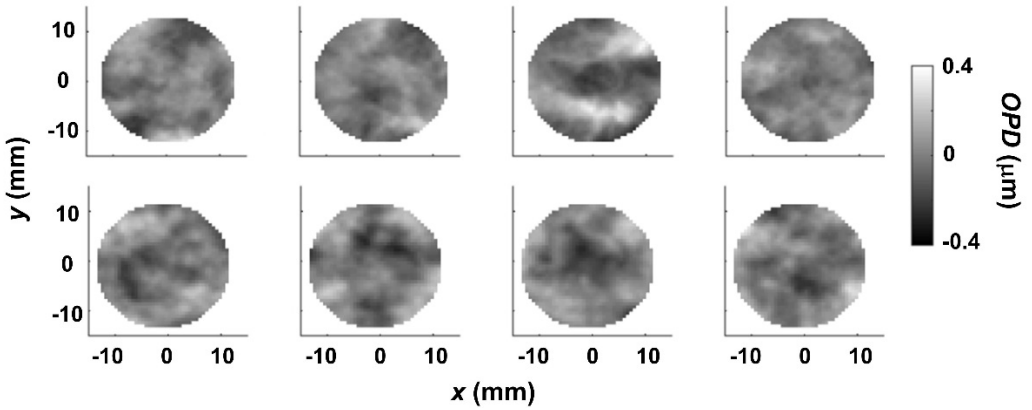

Fig. 8. Examples of wavefronts acquired using LIB spark with Zernike modes 4, 6 and 7 removed (top row) and using CW illumination (bottom row), M_∞ = 3, P_t = 1.4 MPa, δ = 15 mm, d_{AP} = 25 mm.

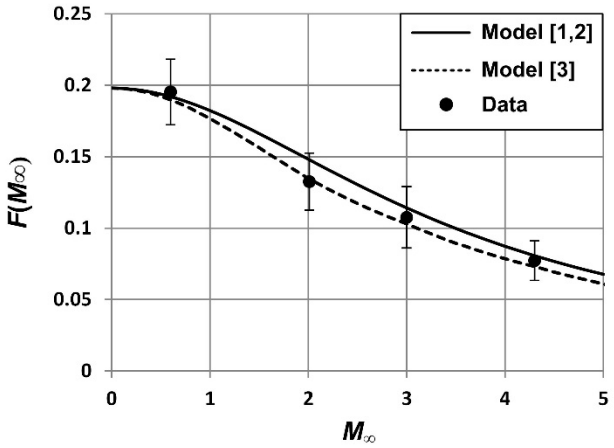

Fig. 9. Empirical function $F(M_\infty)$ for OPD_{rms} of aero-optical effect of flat-plate, adiabatic boundary layer [1 - 3, 15].

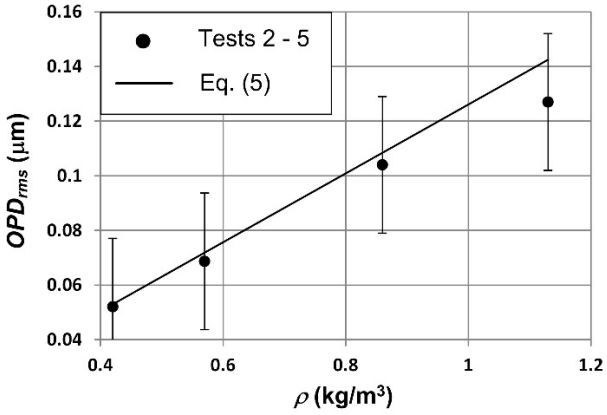

Fig. 10. Spatial OPD_{rms} for tests 2 to 5 in Table 1, with Zernike modes 4, 6 and 7 removed.

B. Deflection-Angle Spatial Spectra

The deflection-angle temporal spectrum is typically calculated from measurements of the motion of one or more small-aperture light beams acquired at sufficiently high sampling rate to resolve the spectral content of the boundary-layer aero-optical effect. However, since the sampling rate of the LIB measurements was limited to 10 Hz by the pulse-repetition rate of the LIB laser, deflection-angle data for the LIB tests were instead estimated from the slope of the wavefront data d*W*/d*x* calculated along the centerline of individual wavefront snapshots in the streamwise direction (after removal of Zernike modes 4, 6 and 7), as depicted in Fig. 11:

$$\theta(x) = \frac{dW(x)}{dx} \tag{6}$$

Deflection-angle (also referred as jitter) spatial spectral densities, $\left|\hat{\theta}(k)\right|^2$, shown in the following figures, are plotted

against the ratio $\delta k/2\pi = \delta/\lambda$, where λ is the wavelength and k is the wavenumber of the aero-optical disturbance. Note that for small-aperture measurements made at high sampling rate, the deflection-angle temporal spectra are instead normally plotted against the Strouhal number based on the sampling frequency St_δ [1-3. 15]; however, the two methods yield essentially the same results with the same spectral behavior, and are simply related by the convection speed, U_c, of aero-optical structures, $\omega = 2\pi f = U_c k$ [1]. From here it is straightforward to show that the normalized streamwise wavenumber, $\delta k/2\pi$, is related to Strouhal number based on δ, as $\delta k/(2\pi) = f\delta/U_c = U_\infty/U_c\, St_\delta$. The ratio U_c/U_∞ is a weak function of the Mach number [15, 20]. For a flat-plate adiabatic boundary layer, $U_c \sim 0.88\, U_\infty$ for $M_\infty = 3$, increasing to $0.9\, U_\infty$ for $M_\infty = 4.38$ [3, 15]. As shown in [20], $\hat{\theta}$ has characteristics that are similar for equilibrium flat-plate boundary-layer flows over a wide range of Mach numbers; specifically, the peak of the spectrum occurs at $St_\delta \sim 1$, or, in wavenumber space, at $\delta k/(2\pi) \sim 1.1$. Thus, the peak location in the spectrum can be used to estimate δ.

Overall aero-optical distortions can subsequently be computed from the spatial spectrum, $OPD_{rms}^2 = \frac{1}{\pi}\int_0^\infty \left|\hat{\theta}(k)\right|^2 dk$.

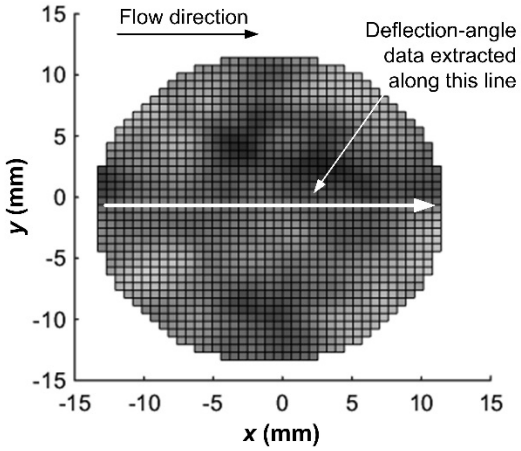

Fig. 11. Diagram illustrating extraction of deflection-angle data from centerline of individual wavefronts.

Deflection-angle spectral densities computed from the LIB data and the CW data are compared in Fig. 12 for $M_\infty = 3$ and in Fig. 13 for $M_\infty = 4.38$. The LIB data in the figures show the ensemble average of 100 to 150 separate jitter measurements with the error bars showing the uncertainty at the 95% confidence level. Note that the maximum wavenumber resolvable by the method is related to the lenslet size in the wavefront-sensor lenslet array giving:

$$\left(\frac{\delta k}{2\pi}\right)_{MAX} = \frac{\delta}{d_L} \tag{7}$$

Similarly, the minimum resolvable wavenumber is:

$$\left(\frac{\delta k}{2\pi}\right)_{MIN} = \frac{\delta}{d_{AP}} \tag{8}$$

The jitter spectra for all tests performed at M_∞ = 3, Tests 2 to 5 in Table 1, are summarized in Fig. 14, which shows how the jitter spectrum shifts due to changes in OPD_{rms} caused by different ρ_∞.

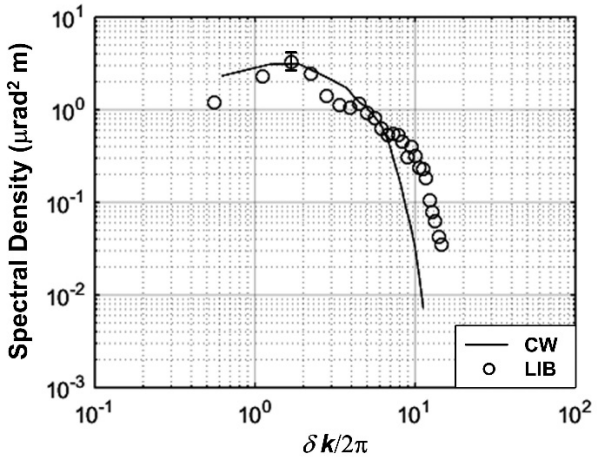

Fig. 12. Deflection-angle spectral densities measured using LIB (with Zernike modes 4, 6, 7 removed) and CW illumination, M_∞ = 3, P_t = 1.0 MPa, d_{AP} = 25 mm.

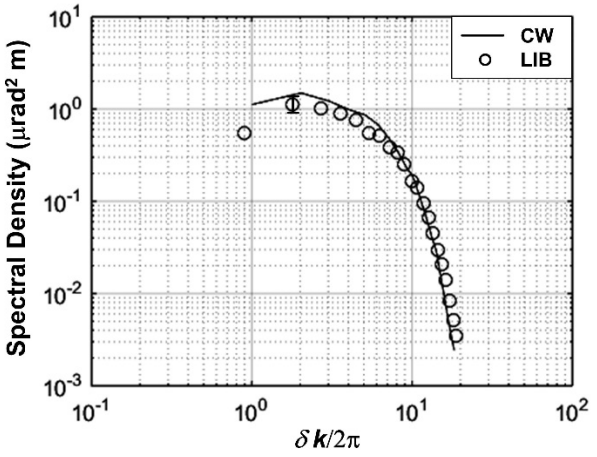

Fig. 13. Deflection-angle spectral densities measured using LIB (with Zernike modes 4, 6, 7 removed) and CW illumination, M_∞ = 4.38, P_t = 1.5 MPa, d_{AP} = 25 mm.

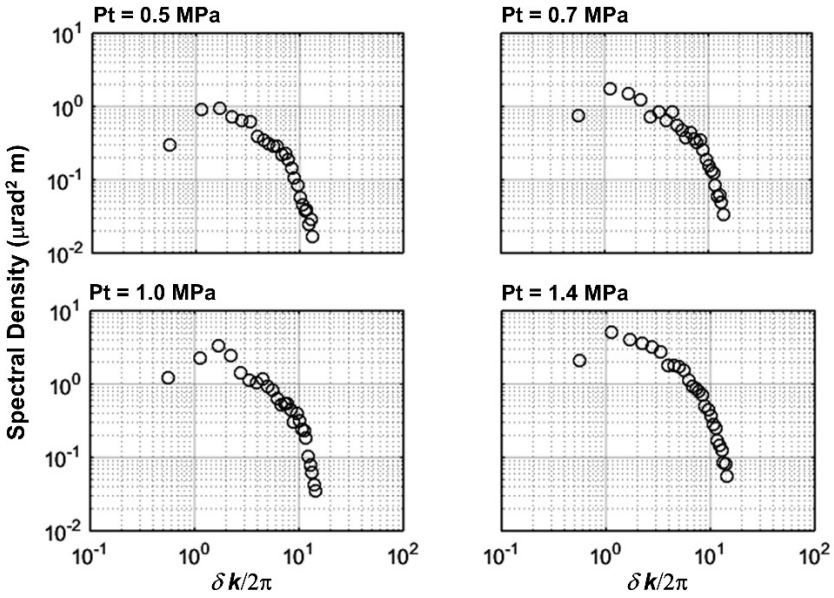

Fig. 14. Deflection-angle spectral densities measured using LIB (with Zernike modes 4, 6, 7 removed) for tests 2 to 5 in Table 1.

Figures 12 and 13 show that the spectral densities computed from the individual LIB wavefronts, after removal of Zernike modes 4, 6 and 7, are generally within experimental uncertainty of the spectra calculated from the CW data. The divergence between the LIB and CW spectra at large wavenumbers visible in Fig. 12 is most likely caused by the lower signal-to-noise ratio of the LIB measurements, which only sampled the wall boundary-layer once and therefore did not have the $2\sqrt{2}$ signal amplification of the CW beam from passing through the test section twice, see Section II. More importantly, Figs. 12 and 13 also show a discrepancy between the LIB and CW spectra at the lowest wavenumbers , especially at M_∞ = 3 (Fig. 12), where the LIB spectra generally show smaller amplitudes than the CW spectra. This discrepancy can be attributed to the removal of the low-order Zernike modes performed to compensate for the effects of LIB spark motion. Figure 15 shows curves extracted along the centerline of the Zernike modes 4, 6, and 7 and clearly illustrates the low-frequency sinusoidal appearance of the modes, so that complete removal of the Zernike modes 4, 6 and 7 from the LIB data may also remove low-frequency components of the actual boundary-layer aero-optical effect. As mentioned previously, the peak of the spectrum occurs at $\delta k/(2\pi) \sim 1.1$ .This means that, in situations where the measurements are performed on an unknown flow in a flight-test environment, the inability to accurately resolve the low-wavenumber components of $\hat{\theta}$ using the LIB spark could compromise the ability to accurately determine the boundary-layer aero-optical effect, especially if the lowest-wavenumber component(s) of $\hat{\theta}$

occur in the range $\delta k/(2\pi) \sim 1$.

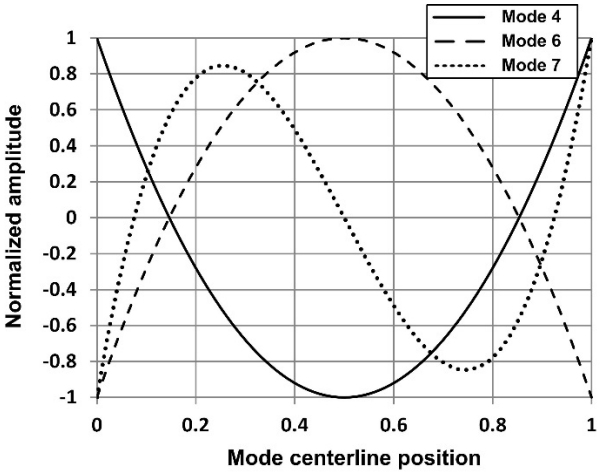

Fig. 15. Normalized plots along centerline of Zernike modes 4, 6, and 7.

The fact that the LIB spectrum in Fig. 13 matches the CW data better than in Fig. 12 was most likely the result of a more-optimum adjustment of the laser pulse energy to produce a smaller LIB spark that had less variation from spark to spark yet was still bright enough for good wavefront measurements. As such, one method of achieving better $\hat{\theta}$ spectra would be to fine tune the laser pulse energy for each test; however, this may not be easily achievable and in any case, would still not eliminate all of the LIB aberrations. Referring to Eq. (8), another method of improving the accuracy of the jitter spectrum in the range $\delta k/(2\pi) \sim 1$ would be to use a large measurement aperture, d_{AP}, which would decrease the ratio δ / d_{AP} and hence shift the Zernike-affected range of the spectrum to lower wavenumbers. However, this option may be impractical for large δ and/or flight-test measurements where space is limited.

An alternative and preferable approach to better resolving the low wavenumber components of $\hat{\theta}$ is to attempt to remove only the part of the Zernike modes 4, 6 and 7 that are actually affected by the spark motion. Referring to Fig.6 it is clear from the CW data that the boundary-layer aero-optical effect contains nonzero magnitudes of the Zernike modes 4, 6 and 7, so that full removal of these modes also removes part of the actual boundary-layer aero-optical signal. In an effort to more accurately account for the effect of the LIB motion, these modes were instead reduced to the levels that would exist normally, that is, the levels measured using the CW illumination. Since the Zernike-mode amplitudes for the LIB and CW data closely match at high mode numbers, this improved estimate of the jitter energy at the lowest St_δ was obtained by extrapolating backwards from the high-order LIB Zernike coefficients to estimate the values of modes 4, 6 and 7 that would exist in the absence of spark motions. This result of this method of estimating

the coefficient magnitudes for modes 4, 6 and 7 is illustrated in Fig. 16, where the curve fit to the higher-order modes was produced by a simple polynomial (in this case, cubic) fit to modes 9 through 40. Note that this method does not predict the sign of the estimated Zernike coefficients 4, 6 and 7; rather, the sign of these modes from the decomposition of the original, raw wavefronts was maintained and only the magnitude of the Zernike modes 4, 6 and 7 was estimated. Despite this limitation, Fig. 17 shows that the method produces an improved approximation of the jitter energy at the lowest frequency of the $\hat{\theta}$ spectrum that more closely matches the CW data.

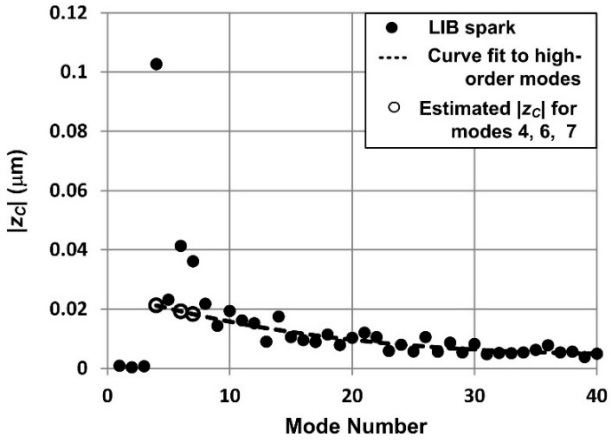

Fig. 16. Method for improved estimate of $|z_C|$ for modes 4, 6, 7.

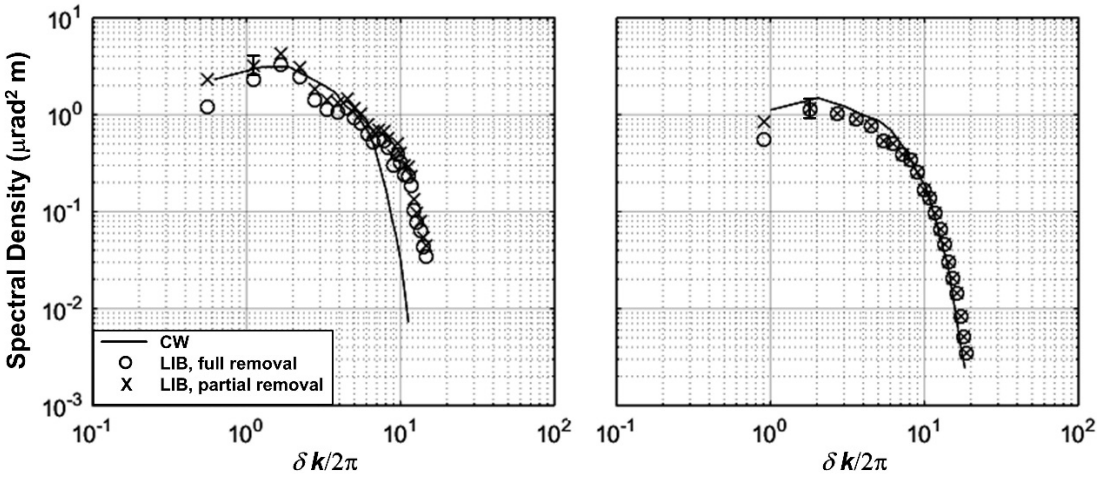

Fig. 17. Deflection-angle spectral densities measured using LIB with full and partial removal of Zernike modes 4, 6, 7 using method of Fig. 16. Left: M_∞ = 3, P_t = 1.0 MPa, d_{AP} = 25 mm. Right: M_∞ = 4.38, P_t = 1.4 MPa, d_{AP} = 25 mm .

IV. Concluding Remarks

The investigation has demonstrated that it is possible to accurately measure the aero-optical effects of flat-plate boundary-layer flows, including OPD_{rms} and deflection-angle spatial spectra, using the light emitted by a LIB spark.

A key step in the measurement technique is the handling of wavefront distortions caused by motion of the LIB spark itself. The investigation has shown that these wavefront distortions can be identified via a Zernike analysis and removed by subtraction of a few low-order Zernike modes, specifically defocus, coma and astigmatism. Other important contributions of the investigation include the complete identification of all Zernike modes affected by the LIB motion and evaluation of their typical magnitudes by comparison with equivalent CW data acquired for the same flow and measurement aperture; these kinds of results have not appeared previously in the literature.

As such, the investigation has shown that after correction for the LIB-induced Zernike modes, it is possible to measure very low optical signals using the LIB spark. Specifically, boundary-layer wavefronts with OPD_{rms} as low as 0.053 μm were successfully measured using the LIB emission, corresponding to the expected aero-optical signal of a flat-plate turbulent boundary layer with δ = 16 mm at an altitude of 9700 m. This is especially significant if it is recognized that the measurements were made with only a single pass of the interrogating LIB light through the boundary-layer flow, in a manner that reproduces the kind of measurement that would be made in an actual flight-test situation. Furthermore, the measurements were performed with the LIB spark formed in the flow, with no observed effect of the flow on the wavefront measurements.

Future efforts should continue to be directed toward methods of mitigating the effect of spark motion, or of eliminating it altogether. For example, there is likely a preferred orientation of the spark with respect to the measurement aperture that minimizes the influence of the spark motion effects on the measured aero-optical data.

Acknowledgments

This work has been supported by the United States Air Force Office of Scientific Research Contract Number FA9550-13-C-0010. The U.S. Government is authorized to reproduce and distribute reprints for governmental purposes notwithstanding any copyright notation thereon. Any opinions, findings and conclusions or recommendations expressed in this material are those of the authors and do not necessarily reflect the views of the AFOSR.

References

[1] Gordeyev, S., Smith, A.E., Cress, J.A., and Jumper, E.J., “Experimental studies of aero-optical properties of subsonic turbulent boundary layers", *Journal of Fluid Mechanics*, Vol. 740, 2014, pp. 214-253.

[2] Gordeyev, S., Jumper, E.J., and Hayden, T.E., "Aero-Optical Effects of Supersonic Boundary Layers," *AIAA Journal*, Vol. 50, No. 3, 2012, pp. 682-690.

[3] Wyckham, C.M., and Smits, A.J., "Aero-Optic Distortion in Transonic and Hypersonic Turbulent Boundary Layers," *AIAA Journal*, Vol. 47, No. 9, 2009, pp. 2158-2168., DOI: 10.2514/1.41453.

[4] Gordeyev, S., Smith, A.E., Cress, J.A., and Jumper, E.J., "Aero-optical measurements in a subsonic, turbulent boundary layer with non-adiabatic walls", *Physics of Fluids*, Vol. 27, 045110, 2015

[5] Rennie, R.M., Duffin, D.A., and Jumper, E. J., "Characterization and Aero-Optic Correction of a Forced Two-Dimensional, Weakly-Compressible Shear Layer," *AIAA Journal*, Vol. 46, No. 11, 2008, pp. 2787-2795.

[6] Vorobiev, A., Gordeyev, S., Jumper, E.J., Gogineni, S., Marruffo, A., and Wittich, D.J., "Low-Dimensional Dynamics and Modeling of Shock-Separation Interaction over Turrets at Transonic Speeds", AIAA Paper 2014-2357, June 2014.

[7] Neal, D.R., Armstrong, D.J., Hedlund, E., Lederer, M., Collier, A., Spring, C., Gruetzner, J., Hebner, G., and Mansell, J., "Wavefront sensor testing in hypersonic flows using a laser-spark guide star," SPIE Proceedings, Vol. 3172, 1997, pp. 349-361.

[8] Rennie, R. M., Whiteley, M. R., Cross, G., Cavalieri, D., and Jumper, E. J., "Optical Measurements of a Compressible Shear Layer Using a Laser-Induced Air Breakdown Beacon," AIAA Paper 2010-1158, Jan, 2010.

[9] Rennie, R.M., Goorskey, D., Whiteley, M.R., Cavalieri, D., and Jumper, E.J., "Evaluation of Laser Beacon for Adaptive-Optic Correction of a Compressible Shear Layer," *AIAA Journal*, Vol. 51, No. 4, 2013, pp. 1008-1011.

[10] Rennie, R.M., Goorskey, D., Whiteley, M.R., and Jumper, E.J., "Wavefront Measurements of a Laser-Induced Breakdown Spark in Still Air," *Applied Optics*, v.51, no.11, 2012.

[11] Rigaut, F. & Gendron, E, "Laser guide star in adaptive optics - The tilt determination problem," *Astronomy and Astrophysics*, Vol. 261, No. 2, 1992, pp. 677-684.

[12] Stratford, B.S. and Beaver, G.S., "The Calculation of the Compressible Turbulent Boundary layer in an Arbitrary Pressure Gradient – A Correlation of Certain Previous Methods," Reports and Memoranda No. 3207, Ministry of Aviation, Aeronautical Research Council, London, 1961.

[13] Svelto, O., *Principles of Lasers*, Plenum Press, New York, 1998.

[14] Tambay, R., Muthu, D.V.S., Kumar, V., and Thareja, R.K., "Laser induced breakdown using 0.355, 0.532, and 1.06 μm radiation," *Pramana J. Phys*., V. 37, No. 2, 1991, pp. 163-166.

[15] Gordeyev, S., Rennie, R.M., Cain, A.B., and Hayden, T.E., “Aero-Optical Measurements of High-Mach Supersonic Boundary Layers,” AIAA Paper 2015-3246, June, 2015.

[16] Nightingale, A.M., and Gordeyev, S., "Shack-Hartmann Wavefront Sensor Image Analysis: A Comparison of Centroiding Methods and Image Processing Techniques”, *Journal of Optical Engineering*, 52(7), 071413, 2013.

[17] Southwell, W. H., “Wave-front estimation from wave-front slope measurements,” *J. Opt. Soc. Am.*, Vol. 70, No. 8, 1980, pp. 998-1006.

[18] Rennie, R.M., Nguyen, M., Gordeyev, S., Cain, A.B., and Hayden, T.E., “Windspeed and Flow Angle Measurement by Tracking of a Laser-Induced Breakdown Spark,” AIAA Paper 2015-2574, 33rd AIAA Applied Aerodynamics Conference, Dallas, TX, June, 2015.

[19] Noll, R.J., “Zernike polynomials and atmospheric turbulence,” *J. Opt. Soc. Am*., Vol. 66, No. 3, 1976, pp.2017-211.

[20] Gordeyev, S., and Juliano, T.J., “Optical Characterization of Nozzle-Wall Mach-6 Boundary Layers,” AIAA Paper 2016-1586, 54th AIAA Aerospace Sciences Meeting, San Diego, CA, January, 2016.